In-vivo characterization of magnetic inclusions in the subcortex from non-exponential transverse relaxation decay

1   **Rita Oliveira[1*], Quentin Raynaud[1], Ileana Jelescu[2], Valerij G. Kiselev[3], Evgeniya Kirilina[4],**

2   **Antoine Lutti[1]**

3   [1]Laboratory for Research in Neuroimaging, Department of Clinical Neuroscience, Lausanne University

4   Hospital and University of Lausanne, Lausanne, Switzerland

5   [2]Department of Radiology, Lausanne University Hospital (CHUV) and University of Lausanne,

6   Lausanne, Switzerland

7   [3]Medical Physics, Department of Radiology, Faculty of Medicine, University of Freiburg, Freiburg,

8   Germany

9   [4]Department of Neurophysics, Max Planck Institute for Human Cognitive and Brain Sciences,

10 Stephanstr. 1a, Leipzig 04103, Germany

11 *** Correspondence:**

12 Rita Oliveira: ana.veiga-de-oliveira@chuv.ch

13 **Abstract**

14 According to theoretical studies, the MRI signal decay due to transverse relaxation, in brain tissue

15 with magnetic inclusions (e.g. blood vessels, myelin, iron-rich cells), exhibits a transition from a

16 Gaussian behaviour at short echo times to exponential at long echo times. Combined, the Gaussian

17 and exponential decay parameters carry information about the inclusions (e.g., size, volume fraction)

18 and provide a unique insight into brain tissue microstructure. However, gradient echo decays obtained

19 experimentally typically only capture the long-time exponential behaviour. Here, we provide

20 experimental evidence of non-exponential transverse relaxation signal decay at short times in human

21 subcortical grey matter, from MRI data acquired in vivo at 3T. The detection of the non-exponential

22 behaviour of the signal decay allows the subsequent characterization of the magnetic inclusions in

23 the subcortex.

24 The gradient-echo data was collected with short inter-echo spacings, a minimal echo time of 1.25 ms

25 and novel acquisition strategies tailored to mitigate the effect of motion and cardiac pulsation. The

26 data was fitted using both a standard exponential model and non-exponential theoretical models

27 describing the impact of magnetic inclusions on the MRI signal. The non-exponential models provided

28 superior fits to the data, indicative of a better representation of the observed signal. The strongest

29 deviations from exponential behaviour were detected in the substantia nigra and globus pallidus.

30 Numerical simulations of the signal decay, conducted from histological maps of iron concentration in

31 the substantia nigra, closely replicated the experimental data – highlighting that non-heme iron can

32 be at the source of the non-exponential signal decay.

33 To investigate the potential of the non-exponential signal decay as a tool to characterize brain

34 microstructure, we attempted to estimate the properties of the inclusions at the source of this decay

35 behaviour using two available analytical models of transverse relaxation. Under the assumption of the

36 static dephasing regime, the magnetic susceptibility and volume fractions of the inclusions was

37 estimated to range from 1.8 to 4 ppm and from 0.02 to 0.04 respectively. Alternatively, under the

38 assumption of the diffusion narrowing regime, the typical inclusion size was estimated to be ~2.4 μm.

39 Both simulations and experimental data point towards an intermediate regime with a non-negligible

40 effect of water diffusion to signal decay. Non-exponential transverse relaxation decay provides new

41 means to characterize the spatial distribution of magnetic material within subcortical grey matter tissue

42 with increased specificity, with potential applications to Parkinson's disease and other pathologies.

43 **Keywords:** transverse relaxation, R_2^*, iron, basal ganglia, non-exponential decay

1   Introduction

The decay of gradient-echo Magnetic Resonance Imaging (MRI) data due to transverse relaxation is widely considered to follow an exponential behaviour with a rate R_2^* (Weiskopf et al., 2014). Estimates of R_2^* correlate with iron concentration within brain tissue (Péran et al., 2009; Yao et al., 2009; Fukunaga et al., 2010; Langkammer et al., 2010), a property of primary importance for the study of the brain. Iron plays a crucial role in various biological processes such as myelin synthesis, energy production, neurotransmitter synthesis and signalling (Hare et al., 2013; Möller et al., 2019). Therefore some cell types including oligodendrocytes, microglia and dopaminergic neurons exhibit elevated cellular iron concentrations. Abnormal accumulation of iron constitutes a hallmark of neurodegenerative disorders such as Parkinson's Disease (Gerlach et al., 1994; Thompson et al., 2001; Ward et al., 2014) and can be monitored non-invasively in patients using R_2^* mapping data (Ulla et al., 2013; Damulina et al., 2020). Empirical models have been proposed to link R_2^* to the overall iron concentration (Schweser et al., 2011; Stüber et al., 2014). However, these models lack a biophysical foundation crucial for specificity, and fail to capture the characteristics of iron-rich cells in the tissue.

Microscopic inclusions of magnetic material within brain tissue such as iron-rich cells, myelin, or blood vessels, induce microscopic inhomogeneities of the magnetic field which can result in a non-exponential gradient-echo signal decay (Haacke et al., 2005; Kiselev and Novikov, 2018). According to theoretical studies, signal decays that result from these magnetic field inhomogeneities display a Gaussian behaviour at short echo times followed by an exponential behaviour at longer echo times (Yablonskiy and Haacke, 1994; Jensen and Chandra, 2000a; Kiselev and Novikov, 2002, 2018; Sukstanskii and Yablonskiy, 2003). Combined, the coefficients that describe the Gaussian and exponential behaviours carry complementary information about those inclusions (e.g., volume fraction, magnetic susceptibility, size). If measured experimentally, these coefficients allow the assessment of the inclusions with improved specificity, offering valuable insights into the cellular underpinnings of neurodegenerative diseases. However, while this non-exponential behaviour has been observed in suspensions of paramagnetic beads (Storey et al., 2015), in ex vivo brain samples (Jensen and Chandra, 2000a), and in vivo blood vessels (Ulrich and Yablonskiy, 2016), no such evidence exists in iron-rich subcortical grey matter.

The characterization of the magnetic inclusions at the source of non-exponential signal decay requires biophysical models of transverse relaxation that establish a quantitative link between the measured MRI data and the properties of the inclusions within brain tissue (e.g. volume fraction, magnetic susceptibility…). These models capture two phenomena. One is the distribution of Larmor frequencies experienced by water molecules due to the microscopic spatial magnetic field inhomogeneities induced by the inclusions (Yablonskiy and Haacke, 1994; Jensen and Chandra, 2000b). These inhomogeneities are static and their effect on the MRI signal is in principle re-focusable using spin-

3

79   echoes. The other is the temporal effects of water diffusion across this inhomogeneous field - which

80   are non-refocusable (Anderson and Weiss, 1953; Jensen and Chandra, 2000a). Both spatial and

81   temporal effects contribute to signal decay (see Kiselev and Novikov, 2018 for a review). However,

82   analytical expressions of the MRI signal may only be derived from these biophysical models under

83   two mutually exclusive limiting cases. In one case (static dephasing regime, SDR), the spatial

84   inhomogeneities constitute the dominant mechanism underlying signal decay (Yablonskiy and

85   Haacke, 1994; Jensen and Chandra, 2000b). In the other (diffusion narrowing regime, DNR), the

86   temporal effects dominate (Anderson and Weiss, 1953; Kennan et al., 1994; Jensen and Chandra,

87   2000a; Kiselev and Novikov, 2002; Sukstanskii and Yablonskiy, 2003).

88   The question of which regime is more suitable to describe the biophysics of transverse relaxation

89   within brain tissue is a topic of debate and depends on the magnetic field strength and brain region

90   under consideration (Sedlacik et al., 2014; Brammerloh et al., 2021; Yablonskiy et al., 2021). In the

91   subcortex, quantitative assessment of iron distribution at the microscopic scale revealed a complex

92   distribution of paramagnetic iron, characterized by a substantial amount dispersed diffusely

93   throughout the tissue, in addition to localized iron-rich cells (Kirilina et al., 2020; Friedrich et al., 2021;

94   Brammerloh et al., 2024). Biophysical models informed by such detailed quantitative measurements

95   have demonstrated that the SDR is suitable to describe the contribution of dopaminergic neurons in

96   the substantia nigra (SN) at field strengths of 7T or above (Sedlacik et al., 2014; Brammerloh et al.,

97   2021). At lower field strengths, diffusion needs to be taken into account (Brammerloh et al., 2024).

98   Because such detailed findings have not been presented for other subcortical nuclei and populations

99   of iron-rich cells, our understanding of which relaxation regime dominates remains fragmented.

100   In this work, we provide experimental evidence of non-exponential MRI signal decay due to transverse

101   relaxation in subcortical brain regions, in gradient-echo data acquired in vivo at 3T. We fitted the signal

102   decay with an empirical expression and with theoretical models of the effect of magnetic inclusions on

103   the MRI signal (Anderson and Weiss, 1953; Yablonskiy and Haacke, 1994; Jensen and Chandra,

104   2000a; Sukstanskii and Yablonskiy, 2003). From the value of the Gaussian and exponential

105   parameters of the signal decay, we estimated the properties of the magnetic inclusions under the

106   assumption of the SDR and DNR. For the SN, these estimates were compared with the microscopic

107   distribution of iron known from analyses of ex vivo brain tissue.

2   Theory

2.1   Transverse relaxation in the presence of magnetic inclusions

110   Differences between existing biophysical models of the effect of magnetic inclusions on transverse

111   relaxation rely mainly involve the dominating dephasing regime (SDR or DNR) and secondary

112   assumptions about the spatial distribution of magnetic material at the microscopic scale. In particular,

4

113 models derived in the DNR for weak magnetic field inhomogeneities differ in the form of the auto-
114 correlation function of the Larmor frequency experienced by diffusing spins over time. In the model of
115 Anderson and Weiss (Anderson and Weiss, 1953) (AW), this auto-correlation function is assumed to
116 take an exponential form. In the model of Sukstanskii and Yablonskiy (Sukstanskii and Yablonskiy,
117 2003) and Jensen and Chandra (Jensen and Chandra, 2000a) (JC), the auto-correlation function was
118 derived analytically from Gaussian water diffusion within the tissue. All existing models predict
119 asymptotic behaviours of the signal decay of the following forms:

120
$$ S \approx S_0 \exp\left(-\frac{1}{2}\langle\Omega^2\rangle T_E{}^2\right)\exp\left(-R_{2,nano}T_E\right)F_{macro}(T_E)\,, \quad T_E \ll \frac{R^*_{2,micro}}{\langle\Omega^2\rangle} \tag{1} $$

121
$$ S \approx S_0 \exp\left(-R^*_{2,micro}T_E\right)\exp\left(-R_{2,nano}T_E\right)F_{macro}(T_E)\,, \quad T_E \gg \frac{R^*_{2,micro}}{\langle\Omega^2\rangle} \tag{2} $$

122 where S_0 is the signal amplitude at $T_E = 0$, $R_{2,nano}$ is the transverse relaxation rate due to spin
123 interactions at the molecular/nanoscopic scale, $F_{macro}(T_E)$ is the effect of macroscopic magnetic field
124 inhomogeneities (Yablonskiy et al., 2013), $\langle\Omega^2\rangle$ is the variance of the field inhomogeneities induced
125 by the magnetic inclusions (Novikov et al., 2018) and $R^*_{2,micro}$ is the transverse relaxation rate induced
126 by the magnetic inclusions at the microscale. A parametric evaluation of these expressions was
127 conducted with a Padé approximation, which is a flexible model-free signal representation (Novikov
128 et al., 2018) derived from a fraction of two polynomials with coefficients adjusted to satisfy the required
129 asymptotic forms at the short- (Gaussian) and long- (exponential) time limits:

130
$$ S_{Padé} = S_0 \exp\left(-\frac{\langle\Omega^2\rangle T_E{}^2}{2\left(1+\frac{\langle\Omega^2\rangle}{2R^*_{2,micro}}T_E\right)}\right)\exp\left(-R_{2,nano}T_E\right)F_{macro}(T_E) \tag{3} $$

131 We also used the AW and JC models after parameterization in terms of $\langle\Omega^2\rangle$ and $R^*_{2,micro}$:

132
$$ S_{AW} = S_0 \exp\left(-\frac{R^*_{2,micro}{}^2}{\langle\Omega^2\rangle}\left(\frac{\langle\Omega^2\rangle}{R^*_{2,micro}}T_E + e^{-\frac{\langle\Omega^2\rangle}{R^*_{2,micro}}T_E} - 1\right)\right)\exp\left(-R_{2,nano}T_E\right)F_{macro}(T_E) \tag{4} $$

133
$$ S_{JC} = S_0 \exp\left(-\frac{R^*_{2,micro}{}^2}{\langle\Omega^2\rangle}\left(\frac{\langle\Omega^2\rangle}{R^*_{2,micro}}T_E - \sqrt{1 + 2\frac{\langle\Omega^2\rangle}{R^*_{2,micro}}T_E} + 1\right)\right)\exp\left(-R_{2,nano}T_E\right)F_{macro}(T_E) \tag{5} $$

134 The exponential approximation of the signal is simply:

135
$$ S_{Exp} = S_0 \cdot \exp(-R^*_2 T_E) \cdot F_{macro}(T_E) \tag{6} $$

136 with $R^*_2 = R^*_{2,micro} + R_{2,nano}$.

137 **2.2 Microscopic underpinnings of non-exponential decay**

5

138 The MRI parameters $R^*_{2,micro}$ and $\langle\Omega^2\rangle$ of the signal decay can be linked to the microscopic properties

139 of the inclusions that contain the magnetic material (e.g. iron-rich cells), assumed to have a spherical

140 shape. In particular, the mean square frequency deviation $\langle\Omega^2\rangle$ of the magnetic field inhomogeneities

141 generated by randomly distributed inclusions is (Yablonskiy and Haacke, 1994; Jensen and Chandra,

142 2000a; Sukstanskii and Yablonskiy, 2003):

143 $$\langle\Omega^2\rangle = \frac{4}{45}\zeta \cdot (1-\zeta)(\gamma B_0 \Delta\chi)^2 \approx \frac{4}{45}\zeta \cdot (\gamma B_0 \Delta\chi)^2 \qquad (7)$$

144 where $\zeta \ll 1$ is the volume fraction of the magnetic inclusions, $\Delta\chi$ is their susceptibility difference with

145 the surrounding tissue (SI units), γ the gyromagnetic ratio ($2.675 \cdot 10^8\ rad\ s^{-1}T^{-1}$) and B_0 the main

146 magnetic field. Note that $\langle\Omega^2\rangle$ is a measure of magnetic field inhomogeneities averaged across an

147 imaging voxel. By contrast, the characteristic Larmor frequency induced by a single sphere is: $\delta\Omega_s =$

148 $\frac{1}{3}\gamma B_0\ \Delta\chi$ (Yablonskiy and Haacke, 1994).

149 In the framework of the SDR (Yablonskiy and Haacke, 1994) and DNR (Jensen and Chandra, 2000a;

150 Sukstanskii and Yablonskiy, 2003), the relaxation rate is described by the following equations:

151 $$R^*_{2,micro} = \lambda_{SDR}\zeta\gamma B_0\Delta\chi, \qquad \lambda_{SDR} = \frac{2\pi}{3\sqrt{3}} \cdot \frac{1}{3} \approx 0.4031 \qquad (8a)$$

152 $$R^*_{2,micro} = \lambda_{DNR}\zeta\gamma^2 B_0^2\Delta\chi^2\tau, \quad \lambda_{DNR} = \frac{16}{75} \approx 0.2133 \qquad (8b)$$

153 where $\tau = \frac{r^2}{6D}$ is the time scale for water molecules to diffuse away from a spherical magnetic inclusion

154 of radius r. D is the water diffusion coefficient in tissue (1 μm²/ms).

155 In the DNR, the dimensionless parameter $\alpha = \tau \cdot \delta\Omega_s \propto r^2$ (Yablonskiy and Haacke, 1994; Kiselev

156 and Novikov, 2002) represents the amount of spin dephasing induced by the field inhomogeneities

157 over the period τ. In the DNR, the condition $\alpha \ll 1$ must be verified. The DNR may therefore apply to

158 distributions of magnetic inclusions with comparatively smaller sizes than the SDR. Note that the

159 relaxation rate of the DNR is parametrically smaller than that of the SDR: $\frac{R^*_{2,micro,DNR}}{R^*_{2,micro,SDR}} = \alpha \frac{\lambda_{DNR}}{\lambda_{SDR}} \approx \alpha/2 \ll$

160 1. As a result, the relaxation rate of the MRI data will yield very different properties of the inclusions

161 $(\Delta\chi, \zeta\ \tau)$ under the SDR and DNR.

162 **3   Methods**

163 **3.1   Participant cohort**

164 MRI data were acquired from 5 healthy volunteers (2 females, mean age=32±9 years old). The study

165 received approval by the local ethics committee and all volunteers gave written informed consent for

166 their participation.

6

3.2 Data acquisition

MRI data were acquired on a 3T whole-body MRI system (Magnetom Prisma; Siemens Medical Systems, Erlangen, Germany) with a 64-channel receive head coil and a custom-made multi-echo 3D fast low-angle shot (FLASH) pulse sequence with bipolar readout. To facilitate the detection of a non-exponential signal decay, 16 gradient-echo images were acquired with a minimal echo time of 1.25 ms, and inter-echo spacing of 1.2 ms. The radio-frequency (RF) flip angle was 12° and the repetition time was 23.2 ms. Image resolution was 1.2 mm³ isotropic, with a field of view 208×192×144 mm along the read and two phase-encode directions. Partial Fourier (factor 6/8) was used in the phase and partition directions. Three repetitions were conducted on each participant and the total nominal acquisition time was 18min09s.

To minimize image degradation due to head motion, an optical tracking prospective motion correction system (KinetiCor, HI, Honolulu) was used (Zaitsev et al., 2006; Maclaren et al., 2012). Cardiac pulsation constitutes an additional source of noise in brain relaxometry data which accounts for up to 35% of the variability of R_2^* maps across repetitions (Raynaud et al., 2023). To minimize the effect of cardiac-induced noise, the cardiac pulsation of the participants was recorded using a finger pulse oximeter and data acquisition was suspended during the systolic period of the cardiac cycle, taken to last for a duration of 300 ms (Raynaud et al., 2023). For a heart rate of 80 beats per minute, this strategy resulted in an increase in scan time by approximately 40%. As a result of these prospective strategies for the correction of head motion and cardiac pulsation, the motion degradation index (Castella et al., 2018; Lutti et al., 2022; Corbin et al., 2023), an index of data quality, lied within a narrow range across participants and did not exceed 3.4 s⁻¹ (Figure S1).

Multi-parameter mapping (Weiskopf et al., 2013) data was acquired to compute maps of the MRI parameter MTsat (magnetization transfer saturation), a semi-quantitative parameter reflecting tissue myelination with improved contrast between tissue classes, allowing an accurate delineation of subcortical grey matter regions (Helms et al., 2009). The protocol comprised three multi-echo 3D FLASH scans acquired with magnetization transfer-, proton density- and T1- weighting (RF excitation flip angle = 6°, 6° and 21°, respectively; repetition time TR=24.5 ms). Eight echo images were acquired for the T1- and proton density-weighted contrasts and six for the magnetization transfer-weighted contrast. Image resolution was 1 mm³ isotropic, and the image field of view was 176×240×256 mm. B1-field mapping data was acquired (4 mm³ voxel size, TR/TE = 500/39.1 ms) to correct RF transmit field inhomogeneity effects on the MTsat maps (Lutti et al., 2010, 2012). For correction of image distortions in the B1 map data, B0-field map data was acquired with a 2D double-echo FLASH, TR=1020 ms, α =90◦, TE1/TE2 = 10/12.46 ms, BW = 260 Hz/pixel, slice thickness = 2 mm. The motion correction system described above was also used here.

3.3   Anatomical imaging processing

MTsat maps were calculated from the magnetization transfer-, proton density- and T1-weighted images with the hMRI toolbox (https://hMRI.info) (Tabelow et al., 2019), as described in (Helms et al., 2008a, 2008b; Weiskopf et al., 2013). MTsat maps were segmented into grey and white matter tissue probability maps using the Statistical Parametric Mapping software (SPM12, Wellcome Centre for Human Neuroimaging, London) (Ashburner and Friston, 2005). A grey matter mask was computed by selecting voxels with a grey matter probability above 0.95. Globus pallidus (GP), putamen, thalamus, and caudate regions of interest (ROI) were defined from the grey matter mask and the regional labels of the Neuromorphometrics atlas (http:// neuromorphometrics.com/). As no label exists for the SN, this region was delineated using an *ad hoc* procedure, from a cuboid placed appropriately in the space of each MTsat map. Within this cuboid, SN voxels were identified from the grey matter voxels labelled as brainstem and ventral diencephalon in the Neuromorphometrics atlas. Beyond subcortical grey matter, the fusiform gyrus was also defined from the grey matter mask and the regional label of the Neuromorphometrics atlas, serving as a reference region with a low concentration in non-heme iron (Haacke et al., 2005).

3.4   Fitting of the transverse relaxation decay

Data were analyzed using bespoke analysis scripts written with MATLAB R2021a (The Mathworks, Natick, MA). The effect of macroscopic magnetic field inhomogeneities on the gradient-echo signal (F_{macro} in Eqs. 1-6) was corrected with the voxel spread function (VSF) method (Yablonskiy et al., 2013). The complex gradient-echo data were denoised using the Marchenko Pastur-PCA method (Veraart et al., 2016b, 2016a; Does et al., 2019), using cubic regions of 5x5x5 voxels. At each voxel, we removed scaling and additive effects between the signal decays acquired across repetitions, due to e.g. head motion in the spatially varying sensitivity profile of the receive coil. To suppress the noise floor in the magnitude images, background voxels outside the head were identified from the segmentation of the first gradient-echo image using SPM12 (Ashburner and Friston, 2005). The distribution of signal intensities across noise voxels was fitted assuming a Rician distribution and the resulting value of the noncentrality parameter was deducted from the signal intensities.

Fitting of the transverse relaxation decay with the analytical expressions of Section 2.1 was conducted using non-linear least square minimization (*lsqnonlin* Matlab function) with a trust-region-reflective algorithm. $R_{2,micro}^*$ was bounded between 1 to 80 s^{-1} with an initial value of 20 s^{-1} for the signal models of Eqs 3-5. The $\langle \Omega^2 \rangle$ parameter ranged from 100 to 4x10^4 $rad^2 s^{-2}$ for the Padé and AW models and from 100 to 8x10^4 $rad^2 s^{-2}$ for the JC model with an initial value of 10^4 $rad^2 s^{-2}$ for all of them. R_2^* from Eq. 6 ranged from 0 to 80 s^{-1} with an initial value of 20 s^{-1}. S_0 was bounded between 10 and 2000 with an initial value of 500. $R_{2,nano}$ was not estimated during data fitting due to the unsuitable range of echo

8

235   times of the data and was set to 10 s^{-1} instead (Jensen and Chandra, 2000a; Sedlacik et al., 2014;

236   Brammerloh et al., 2021). As $R_{2,nano}$ depends on tissue iron concentration, this carries the risk of

237   misattributing the actual value of $R_{2,nano}$ to $R^*_{2,micro}$.

238   While the Padé expression is not strictly speaking a model but a representation of the MRI signal, we

239   henceforth refer to all three analytical expressions (Eqs. 3-5) as models of the MRI signal for the sake

240   of simplicity. The goodness of fit of each model was estimated from the mean squared error of the fit

241   (MSE) and the Akaike Information Criterion (AIC), which includes a penalty for model complexity.

242   Lower MSE and AIC values indicate a better model fit. Model parameter estimates for the five regions

243   of interest were extracted from all voxels and all subjects after the removal of the voxels with high

244   MSE (>15), indicative of spurious effects in the data such as physiological noise (as reference the

245   average MSE across all voxels is ~8). We also excluded voxels where the transition from Gaussian

246   to exponential behaviour took place over a timescale $\frac{R^*_{2,micro}}{\langle \Omega^2 \rangle} < 0.5$ ms after RF excitation, too short to

247   be robustly detectable.

3.5   Microscopic underpinnings of non-exponential decay

249   From the estimates of $R^*_{2,micro}$ and $\langle \Omega^2 \rangle$ et each voxel, we attempted to estimate the properties of the

250   magnetic inclusions at the source of the non-exponential decay within brain tissue. This analysis was

251   conducted under the two mutually exclusive scenarios of the SDR and DNR, each providing a different

252   interpretation of the decay curve parameters in terms of microstructural tissue properties.

253   Under the assumption of the SDR, we estimated the magnetic susceptibility ($\Delta\chi$) and volume fractions

254   (ζ) of the inclusions (Eqs. 7 and 8a). Under the assumption of the DNR, where diffusion effects are

255   considered, the model parameters $R^*_{2,micro}$ and $\langle \Omega^2 \rangle$ depend not only on $\Delta\chi$ and ζ as in the SDR, but

256   also on τ. Since all three properties cannot be estimated separately from $R^*_{2,micro}$ and $\langle \Omega^2 \rangle$ alone, only

257   τ was estimated (Eqs. 7 and 8b).

258   We conducted non-parametric Kruskal-Wallis statistical tests of inter-regional differences in the

259   estimates of $\Delta\chi$ and ζ obtained under the assumption of the SDR (*kruskalwallis* function in Matlab

260   2021). Post-hoc Tukey's HSD tests were conducted subsequently to identify the pairs of regions at

261   the source of these differences (*multcompare* function in Matlab). The effect size was computed using

262   the cliff's delta to quantify the magnitude of differences between regions.

3.6   Non-heme iron as a possible source of the non-exponential signal decay

264   To investigate if the detected non-exponential decay can be induced by microscopic inclusions of non-

265   heme iron with cellular sizes, we numerically simulated the gradient-echo signal decay induced by

266   iron-rich cells of the SN at 3T. The numerical simulations were conducted from the cellular distribution

267   of iron in neuromelanin-pigmented dopaminergic neurons within the volume of a typical MRI voxel,

268   quantified in 3D with microscopic resolution from a post-mortem brain (Brammerloh et al., 2021), and

269   estimates of the magnetic susceptibility of iron and neuromelanin determined using a combination of

270   MRI microscopy and micro X-ray fluorescence (Brammerloh et al., 2024).

271   The 3D iron distribution was converted into magnetic susceptibility maps using the estimates of

272   neuromelanin magnetic susceptibility obtained experimentally and literature values for ferritin, as

273   described in (Brammerloh et al., 2021, 2024). These maps were convolved with a magnetic dipole

274   kernel to compute the Larmor frequency distribution within this voxel due to the presence of iron and

275   neuromelanin. We then used two methods to simulate the gradient-echo signal decay generated by

276   this frequency distribution: 1) the SDR approximation; and 2) Monte Carlo simulations accounting for

277   water diffusion using a typical water diffusion coefficient of brain tissue of 1 μm^2/ms. The decay

278   resulting from the Monte Carlo simulations was fitted with an exponential for TE > 10 ms and with Eq.

279   3 for all echoes.

280   **4   Results**

281   **4.1   Non-exponential transverse decay in subcortical tissue**

282   At short echo times (T_E <5-10ms), transverse signal decays in the basal ganglia and thalamus (Figure

283   1) display systematic deviations from exponential behaviour: the logarithm of the signal exhibits an

284   initial quadratic form, with a transition towards a linear dependence only at longer times. This

285   behaviour is consistent with the effect of magnetic inclusions (e.g iron-rich cells, myelin, or blood

286   vessels) on the MRI signal predicted by theoretical studies (see (Kiselev and Novikov, 2018) for a

287   review).

288
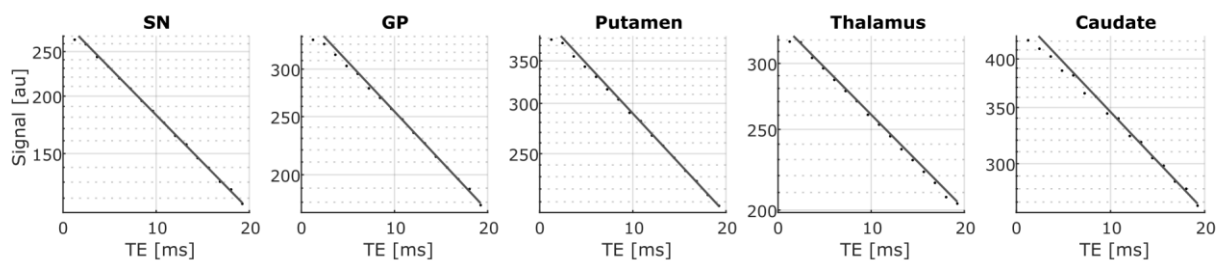
289   **Figure 1.** Transverse relaxation decays in one representative voxel of each subcortical grey matter

290   region (semilog-scale). The line shows the exponential decay fit at long echo times (T_E>10ms). At

291   short echo times (TE≲5ms), the data deviates from the exponential decay fit (line), displaying a

292   quadratic decay consistent with the effect of magnetic inclusions on the MRI signal predicted by the

293   theory.

10

294 The non-exponential models of transverse relaxation (Padé, AW, JC) can account for the non-
295 exponential decay of the MRI signal at short times, leading to an improved fit of the data (Figure 2A).
296 The residual levels are largely consistent across the non-exponential models (MSE ~5), a factor of
297 ~1.6 smaller than for the exponential fit (MSE ~8) (Figure 2B). Similarly, the AIC decreases by a factor
298 of ~1.2 between the exponential (AIC ~100) and non-exponential fits (AIC~90) (Figure 2C), showing
299 that the residual decrease goes beyond that expected from the higher number of parameters of non-
300 exponential models.

301
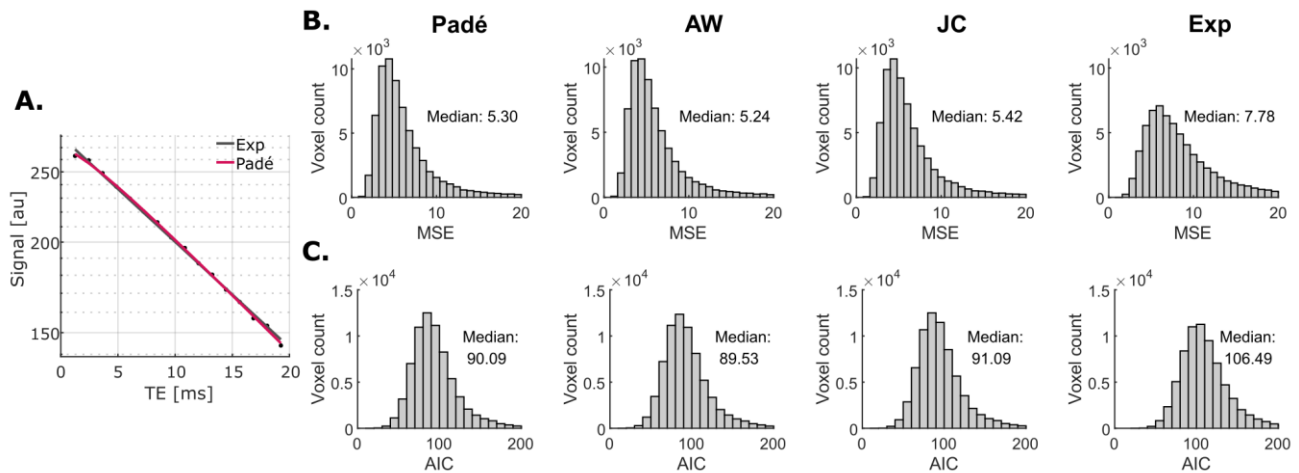
Figure 2. Residual levels across signal models for all subcortical regions analyzed. Example fit for a
representative voxel in the SN (semilog-scale). Non-exponential models of transverse relaxation
(Padé, AW, JC) can account for the non-exponential decay at short times, leading to an improved fit
of the data (A). As a result, the median of residual levels (MSE) is reduced by ~1.6 across subcortical
regions, consistently for all non-exponential models (B). This residual decrease leads to a decrease
of the median AIC by ~1.2, beyond that expected from the higher number of parameters of non-
exponential models (C).

309 The ratio of the MSE between the exponential and non-exponential fits is higher in subcortical regions
310 (average ~1.6) than in cortical grey matter (average ~1.4, Figure 3A and 3B), showing that the non-
311 exponential behaviour takes place predominantly there. In particular, this ratio takes a value of 2 in
312 the iron-rich GP and a value of 1.3 in the iron-poor fusiform gyrus (Haacke et al., 2005). Figure 3C
313 shows example signal decays from these two regions.

11
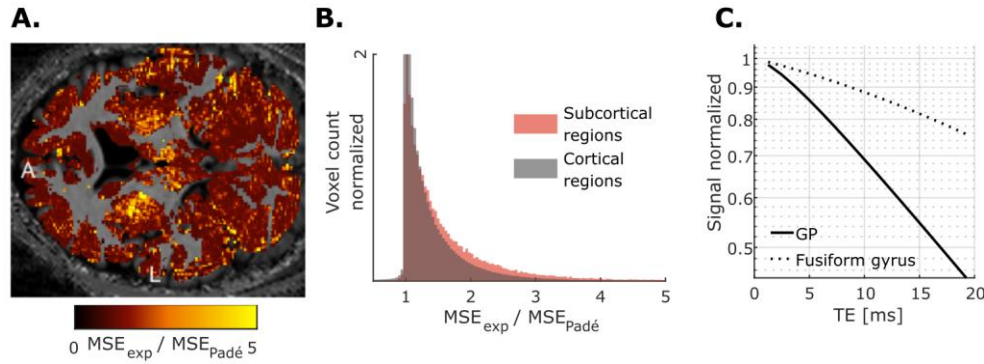
Figure 3. Spatial distribution of the ratio of the MSE obtained from the fits with the exponential and Padé signal models (A). The higher ratio values in subcortical regions (average ~1.6) indicate that stronger deviations from exponential behaviour take place in these areas (B). The stronger non-exponential behaviour in the iron-rich GP than in the iron-poor fusiform gyrus is illustrated for a representative voxel (C, semilog-scale). L – left; A – anterior.

4.2 Estimates of the MRI signal model parameters

Non-exponential signal decays were reliably detected with $\frac{R^*_{2,micro}}{\langle \Omega^2 \rangle}$ >0.5 ms in 71/81/82/83/77/18% of voxels in the SN/GP/putamen/thalamus/caudate/fusiform gyrus, respectively. In these voxels, the non-exponential models (Padé, AW, JC) lead to estimates of $R^*_{2,micro}$ that are respectively 37%, 30%, and 54% higher than the exponential approximation (Figure 4A).
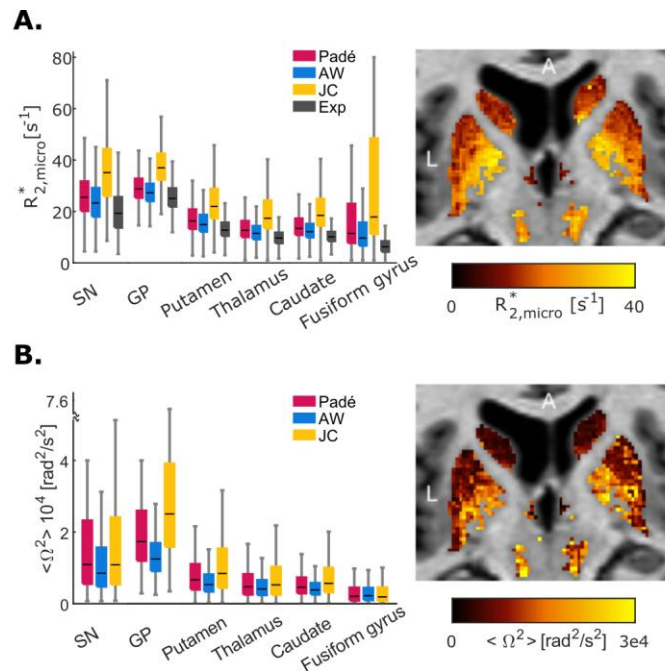

Figure 4. Non-exponential model parameter estimates. Estimates of $R^*_{2,micro}$ (A) and $\langle \Omega^2 \rangle$ (B) are highest in the GP followed by the SN and lowest in the fusiform gyrus, in agreement with histological measures of iron concentration (Hallgren and Sourander, 1958) and Eqs. 7 and 8. The example maps

12

329   of $R^*_{2,micro}$ and $\langle\Omega^2\rangle$ were obtained from the AW model. L – left; A – anterior; Cau – caudate; Put –

330   putamen; GP – globus pallidus; Thal – thalamus; SN – substantia nigra.

331   The estimates of $R^*_{2,micro}$ and $\langle\Omega^2\rangle$ are spatially organized and are consistent between anatomical

332   regions (Figure 4). The values of $R^*_{2,micro}$ and $\langle\Omega^2\rangle$ are higher in the GP and the SN, and lowest in the

333   fusiform gyrus, in agreement with histological measures of iron concentration in brain tissue (Hallgren

334   and Sourander, 1958) and with the expected dependence of these parameters on iron content (Eqs.
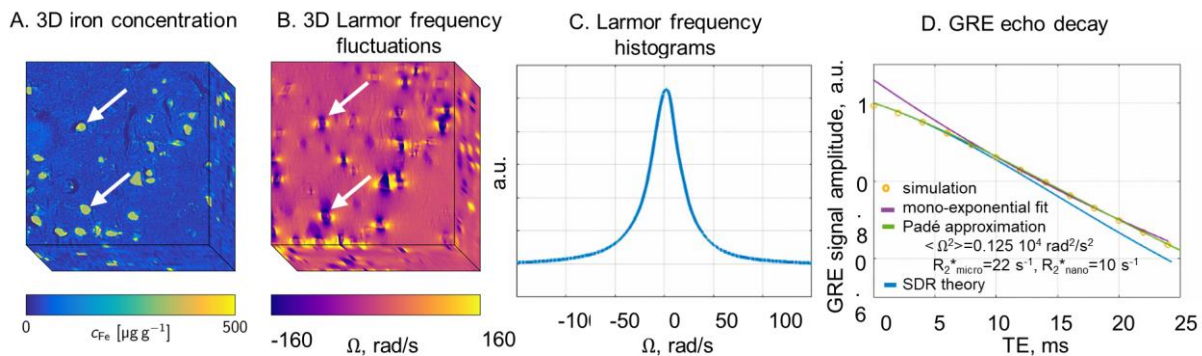
335   7 and 8).

336   The JC model yields systematically higher values of $R^*_{2,micro}$ and $\langle\Omega^2\rangle$ than the AW model and Padé

337   approximation (~31-73%). This arises from the square-root term in the JC signal equation (Eq. 5),

338   which introduces a broad modulation of the signal over the range of echo times of the data (TE < 20

339   ms), i.e. a slow transition to a monoexponential decay. As a result, the decay rate of the data at TE

340   ~10-20ms differs from the estimates of $R^*_{2,micro}$ at TE → ∞ provided by the JC model: the decay of the

341   data and that of the exponential part of the JC fit have different slopes (Figure 5). On the other hand,

342   the estimates of $R^*_{2,micro}$ from the AW model match the decay rate of the data at TE ~10-20ms. Results

343   from the Padé approximation and the AW model are largely consistent.

344
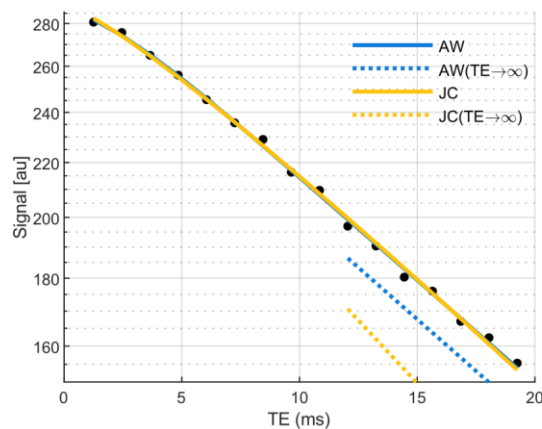
Figure 5. Example transverse relaxation decay from a voxel in the SN and corresponding fits with the AW (blue solid line) and JC (yellow solid line) models (semi-log scale). For each model, the asymptotic behaviour (TE → ∞) plotted as in (Kiselev and Novikov, 2018) (dashed lines), reflects the estimates of $R^*_{2,micro}$. For the AW model, the slope of the experimental data at TE ~10-20ms matches that of the asymptotic behaviour. This is not the case for the JC model due to the square-root term in the JC signal equation: the $R^*_{2,micro}$ estimates provided by the JC model are higher than the decay rate of the data at TE ~10-20ms.

352   **4.3   Non-heme iron as a possible source of the non-exponential signal decay**

13

353   Post-mortem studies of the microscopic cellular distribution of iron in SN demonstrate that
354   dopaminergic neurons accumulate high levels of iron stored in neuromelanin (Figure 6A) (Brammerloh
355   et al., 2021). In adult human brains, these neuromelanin clusters are about 15 μm in radius and contain
356   approximately 300-1000 μg/g of iron (Figure 6A). At 3T, the Larmor frequency perturbations that arise
357   from these paramagnetic inclusions (Figure 6B) lead to a frequency distribution with a width of
358    $\Delta\Omega \sim 35\ rad\ s^{-1}$ (Eq. 7) across the volume of an MRI voxel (Figure 6C). The gradient-echo signal
359   decay that results from these field inhomogeneities using Monte Carlo simulations or the SDR, exhibits
360   a deviation from an exponential behaviour at short echo times (TE < 5 ms, see Figure 6D) consistent
361   with the experimental data (Figure 1). At long echo times, the Monte Carlo simulated signal decay
362   differs from the SDR predictions, suggesting that diffusion effects cannot be ignored for dopaminergic
363   neurons in the SN at 3T. The Monte Carlo simulated decay is better fitted with the Padé model
364   ($R^*_{2,micro} = 22 s^{-1}$, $\langle\Omega^2\rangle = 0.125\ 10^4\ rad^2 s^{-2}$) than with an exponential, similar to our experimental
365   data (Figure 2,4).

A. 3D iron concentration   B. 3D Larmor frequency fluctuations   C. Larmor frequency histograms   D. GRE echo decay

366

367   **Figure 6.** Iron-rich dopaminergic neurons lead to non-exponential signal decay in the SN at 3T.
368   Microscopic iron concentration map obtained from a post-mortem brain (A, adapted from (Brammerloh
369   et al., 2021) under the Creative Commons Attribution 4.0 International License), featuring hotspots of
370   iron accumulation inside dopaminergic neurons, as well as diffusely distributed iron outside the
371   neurons. These paramagnetic inclusions lead to local inhomogeneities of the Larmor frequency (B,
372   adapted from (Brammerloh et al., 2021) under the Creative Commons Attribution 4.0 International
373   License). As a result, a distribution of $\Delta\Omega \sim 35\ rad\ s^{-1}$ of the Larmor frequency takes place across the
374   volume of an MRI voxel (C). The resulting Monte Carlo (circles) and SDR (blue line) simulated
375   gradient-echo signal decays (D) deviate from an exponential at short echo times (TE<5ms),
376   consistently with the experimental data (Figure 1). At long echo times (TE>10 ms), neglecting water
377   diffusion (SDR) leads to a higher exponential decay rate than when water diffusion is accounted for
378   (Monte Carlo simulation). The Padé approximation (green line) provides a better fit to the Monte Carlo
379   simulated signal ($R^*_{2,micro} = 22 s^{-1}$, $\langle\Omega^2\rangle = 0.125\ 10^4\ rad^2 s^{-2}$) than the exponential model (purple
380   line).

4.4 Characterization of magnetic inclusions within subcortical tissue

From the estimates of the MRI signal parameters $R^*_{2,micro}$ and $\langle\Omega^2\rangle$, we characterized the properties of the magnetic inclusions present within brain tissue, at the source of the non-exponential decay under two mutually exclusive scenarios – the SDR and DNR.

Scenario 1: Under the assumption of the SDR (Figure 7), the estimates of $R^*_{2,micro}$ and $\langle\Omega^2\rangle$ were used to estimate the volume fraction (ζ) and magnetic susceptibility ($\Delta\chi$) of the inclusions (Eqs. 7 and 8a). In subcortical grey matter, the median value of $\Delta\chi$ ranges from 1.8 to 4.0 ppm - largest in the GP and SN (~2.6 ppm and 2.4 ppm respectively for the AW signal model), followed by the putamen and thalamus ($\Delta\chi$~2.0 ppm) and caudate ($\Delta\chi$~1.8 ppm). The fusiform gyrus of the cerebral cortex yields the lowest values of $\Delta\chi$ (~1.5 ppm). The GP and SN show the largest values of ζ (median: 0.034 and 0.030 from the AW signal model respectively), followed by the putamen (0.023), caudate (0.021), fusiform gyrus (0.018) and thalamus (0.016). The JC model yields estimates of $\Delta\chi$ that are similar to those of the Padé model and approximately 25% higher than those from the AW model. Additionally, the JC model yields estimates of ζ that are about 54% higher compared to the Padé model and approximately 85% higher compared to the AW model. These differences are due to the systematic differences in the $R^*_{2,micro}$ and $\langle\Omega^2\rangle$ estimates highlighted above.
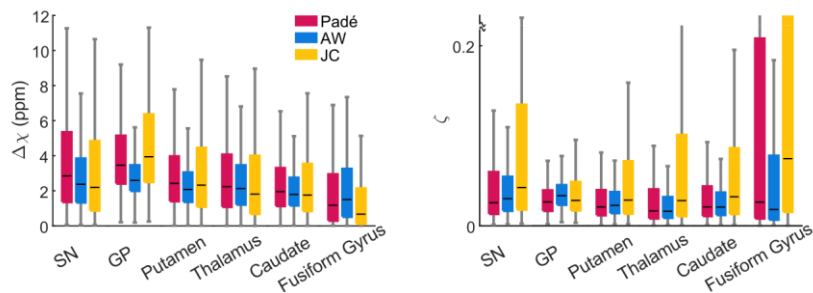

Figure 7. Magnetic susceptibility and volume fractions of magnetic inclusions within brain tissue, estimated from the values of $R^*_{2,micro}$ and $\langle\Omega^2\rangle$ under the assumption of the SDR. Magnetic susceptibilities are larger in the SN and GP (median $\Delta\chi$~2.5 ppm) compared to the remaining regions ($\Delta\chi$~1.6 ppm). The volume fraction of the inclusions (ζ) ranges between ~0.016 and 0.043 across subcortical regions.

The Kruskal-Wallis tests revealed statistically significant differences in $\Delta\chi$ between at least two ROIs ($F_{(5,76596)}$ = [1579], $p < 0.001$ for the AW model). The corresponding Tukey's HSD test for multiple comparisons found significant differences between $\Delta\chi$ estimates from all ROIs ($p<0.01$) with small effect sizes, except between the thalamus and putamen where no significance was found. The fusiform gyrus showed the strongest effect sizes (0.12-0.35) compared to the remaining regions.

15

408 Similarly, the Kruskal-Wallis tests revealed statistically significant differences in ζ between at least two

409 ROIs (F(5,76596) = [1744], p < 0.001 for the AW model). The corresponding Tukey's HSD test showed

410 significant differences between the ζ estimates from the GP and those from the putamen, thalamus,

411 and caudate and between SN and thalamus with the largest effect size (>0.30). Other inter-regional

412 differences were found significant (p<0.01) with small effect sizes (<0.20). A detailed overview of this

413 statistical evaluation can be found in Figure S2.

414 Scenario 2: Under the assumption of the DNR, which for a given $R^*_{2,micro}$ and $\langle \Omega^2 \rangle$, requires a greater

415 total amount of iron compared to the SDR, we estimated the parameter τ according to Eqs. 7 and 8b

416 (Figure 8). The estimates of τ are larger in the fusiform gyrus (median ~2.0 ms, from the Padé signal

417 model), followed by the putamen, thalamus, and caudate (median ~1.0 ms), and finally the SN and

418 GP (median ~0.8 ms). A value of τ~1.0 ms implies a value of ~2.4 μm for the magnetic field

419 inhomogeneities generated by the inclusions. In the fusiform gyrus, this radius is ~3.5 μm (τ~2.0 ms).

420 The JC model yields estimates of τ higher than the Padé model by 26% and than the AW model by

421 35%, due to the systematic differences in the $R^*_{2,micro}$ and $\langle \Omega^2 \rangle$ estimates highlighted above.
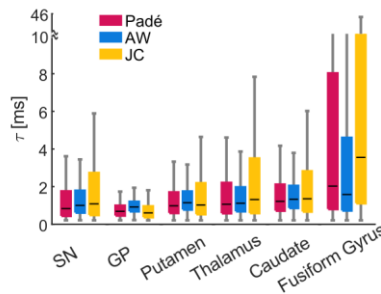
422

423 **Figure 8.** Estimates of the parameter τ, computed from the values of $R^*_{2,micro}$ and $\langle \Omega^2 \rangle$ under the

424 assumption of the DNR. The characteristic diffusion times τ are larger in the putamen, thalamus, and

425 caudate (median ~1.0 ms) compared to SN and GP (~0.8 ms). The fusiform shows the largest values

426 of τ (~2.0 ms).

427 **5   Discussion**

428 Here we provide experimental evidence of non-exponential signal decay due to transverse relaxation

429 in *in vivo* MRI data from subcortical regions. This signal decay follows a Gaussian behaviour at short

430 echo times with a transition to exponential behaviour at long echo times. This non-exponential decay

431 is in agreement with theoretical models of the effect of microscopic magnetic inclusions, located within

432 brain tissue, on the MRI signal. These models show an improved fit to the data compared to the widely

433 used exponential model. The strongest deviations from exponential behaviour are found in iron-rich

434 areas such as the GP and SN. From the values of the model parameters, we estimated the properties

435 of the magnetic inclusions. Numerical simulations of the gradient-echo signal from post-mortem maps

16

436 of iron-rich dopaminergic neurons in SN show that cells rich in non-heme iron can be at the source of

437 this decay behaviour. These results illustrate how non-exponential transverse relaxation signal decay

438 can be used to characterize iron-rich microscopic inclusions from in vivo MRI data.

5.1 Non-exponential transverse relaxation decay

440 The lack of evidence for non-exponential signal decay in subcortical regions has been attributed to

441 the short timescale of the transition between the Gaussian and exponential behaviours, below the

442 range of achievable echo times (Yablonskiy et al., 2021). Here, we combined a dense sampling of the

443 decay curve with acquisition strategies that mitigate the level of physiological noise in the data

444 (Castella et al., 2018; Raynaud et al., 2023) to enable the reliable detection of the non-exponential

445 decay curve. Transverse relaxation decay exhibits a Gaussian behaviour at short echo times

446 ($T_E \lesssim 5ms$) with a transition towards exponential decay (Figure 1), consistent with theoretical models

447 of the effect on the MRI signal of magnetic inclusions within brain tissue (Kiselev and Novikov, 2002;

448 Novikov and Kiselev, 2008). These models show an improved fit to the data compared with the widely

449 used exponential model (Figure 2). This behaviour was predominantly observed in subcortical grey

450 matter regions (Figure 3), known for their elevated non-heme iron content. In particular, the strongest

451 non-exponential behaviours (i.e. higher values of $R^*_{2,micro}$ and $\langle \Omega^2 \rangle$) were observed in GP and SN, the

452 areas with the highest iron content (Figure 4) (Hallgren and Sourander, 1958; Haacke et al., 2005;

453 Langkammer et al., 2012; Krebs et al., 2014). While heme-iron in blood vessels may also contribute

454 to the non-exponential decay, information on its spatial distribution within the tissue remains scarce.

455 Myelin, on the other hand, may have a particularly pronounced effect on the thalamus due to its

456 comparatively high myelin content and low iron concentrations (Hallgren and Sourander, 1958).

457 Transverse relaxation decays obtained from numerical simulations of the gradient-echo signal from

458 post-mortem maps of iron-rich neurons in SN showed the same features as the MRI data acquired

459 experimentally. These findings underscore the contribution of cells rich in non-heme iron to non-

460 exponential signal decay in subcortical grey matter.

461 We considered a model-free Padé approximation and two models of the MRI signal generated by

462 brain tissue with magnetic inclusions. All corresponding expressions fitted the data equally well, with

463 marginal differences between them (Figure 2). Nonetheless, the JC model yields higher estimates of

464 $R^*_{2,micro}$ and $\langle \Omega^2 \rangle$ compared to the AW model and Padé approximations. This discrepancy originates

465 from the long transition from the Gaussian to exponential behaviours predicted by the JC model, due

466 to the square-root term in Eq. 5. As a result, the estimates of $R^*_{2,micro}$ from the JC model differ from

467 the decay rate of the data at TE~10-20ms (Figure 5).

5.2 Characterization of magnetic inclusions within subcortical tissue

469 From the estimates of the two signal model parameters ($R^*_{2,micro}$ and $\langle\Omega^2\rangle$), we attempted to estimate

470 the properties of the magnetic inclusions embedded within brain tissue, which would not have been

471 achievable from the exponential tail of the decay alone. This was conducted under two mutually

472 exclusive scenarios 1) the SDR (Figure 7) and 2) the DNR (Figure 8), each with distinct analytical

473 expressions to quantitatively link the signal model parameters with the properties of the underlying

474 magnetic inclusions.

475 Scenario 1: Under the assumption of the SDR, the estimates of the magnetic susceptibility of the

476 inclusions, lie in the range $\Delta\chi \sim$1.8-4 ppm across subcortical regions and models of the MRI signal.

477 The largest values of $\Delta\chi$ are encountered in the GP and SN, followed by the putamen, thalamus and

478 caudate in decreasing order (2.6, 2.4, 2.0, 2.0, 1.8 ppm respectively for the AW model). This ordering

479 follows that of ex vivo measures of bulk iron concentration within the tissue ($C_{GP} \geq$

480 $C_{SN} > C_{Putamen} > C_{Caudate} > C_{Thalamus}$) (Hallgren and Sourander, 1958; Griffiths et al., 1999; Haacke

481 et al., 2005).

482 The estimates of $\Delta\chi$ derived from the MRI data can be compared with those obtained from ex vivo

483 studies of non-heme iron distribution. In the SN we can assume that the non-exponential relaxation is

484 induced mainly by iron bound to neuromelanin in dopaminergic neurons. In this case, $\Delta\chi =$

485 $\rho \cdot \chi_{eff\_NM} \cdot [Fe]_{NM}$, where $\rho \sim$1.05 g/cm³ (Barber et al., 1970) and $\chi_{eff_NM} \sim$2.98 ppm m³/kg is the

486 effective magnetic susceptibility of neuromelanin (Brammerloh et al., 2024). Taking $[Fe]_{NM} \sim$0.49 mg/g

487 for the concentration of iron in the neuromelanin of dopaminergic neurons (Brammerloh et al., 2021,

488 2024; Friedrich et al., 2021) one gets: $\Delta\chi \sim$1.5 ppm. These estimates are consistent with the ones

489 obtained from our MRI data (2.4 ppm with the AW model). Since quantitative histological data for

490 other regions are unavailable, we cannot verify the plausibility of our model estimates in those areas.

491 The estimates of $\Delta\chi$ derived from the MRI data differ from the magnetic susceptibility of heme iron in

492 blood capillaries (0.4 to 0.5 ppm (Schenck, 1992; Spees et al., 2001)).

493 The estimates of the volume fraction of the inclusions computed from the MRI data lie in the range $\zeta \sim$

494 0.02-0.04 across regions and MRI signal models. In particular, in the SN they are ~0.03 (with the AW

495 model), close to those estimated from histological analyses of the dopaminergic neuron's volume

496 fraction (0.03 to 0.12 (Brammerloh et al., 2021)). The MRI-derived estimates of ζ are also in line with

497 the human capillary vascular volume fraction ($\sim$0.02-0.025 (Buschle et al., 2018)).

498 Scenario 2: Under the assumption of the DNR, we estimated the parameter τ, the decay time of the

499 frequency auto-correlation of water molecules diffusing through the inhomogeneous magnetic field

500 generated by the inclusions. The τ estimates (~1.0 ms) in subcortical grey matter suggest a typical

501 radius r of ~2.4 μm for the magnetic inclusions. This estimate is consistent with the radius of the

502 spherical inclusions reported in other MRI relaxometry studies of excised human grey matter tissue

503 (Jensen and Chandra, 2000a). In particular, the latter study also reported larger values of r in the

18

504 putamen (3.1 μm) , thalamus (3.0 μm), and caudate (2.9 μm), compared to the GP (2.3 μm) as

505 observed here (Figure 8). The MRI-derived estimate of r is also in the order of a small capillary size

506 (~3.2 μm (Lauwers et al., 2008)). However, it is also lower than the typical radius of neuronal or glial

507 cells (5-20 μm in neurons, 5-10 μm in microglia, 2.5-10 μm in astrocytes, 2-5 μm oligodendrocytes

508 (Ward et al., 2014; Reinert et al., 2019; Brammerloh et al., 2021; Friedrich et al., 2021)). The separate

509 estimation of $\Delta\chi$, ζ and τ in the DNR, which can involve estimates of MRI susceptibility in addition to

510 the MRI parameters $R_{2,micro}^*$ and $\langle\Omega^2\rangle$ used here, may help clarify the validity of this assumption.

511 Indeed, the condition $\alpha = \tau \cdot \delta\Omega_s \ll 1$ must be verified in the DNR. Also, because the relaxation rate

512 of the DNR is parametrically smaller than that of the SDR $\left(\frac{R_{2,micro,DNR}^*}{R_{2,micro,SDR}^*} \ll 1\right)$, the resulting estimates of

513 $\Delta\chi$ and ζ may differ greatly from those presented here.

514 In conclusion, while the SDR may be plausible in the SN, this may not be the case in other regions.

515 Instead, the most plausible scenario may be that transverse relaxation results from an intermediate

516 dephasing regime, between these limiting cases. Therefore, approaches that interpolate between

517 these two limiting cases may allow a more accurate characterization of the magnetic inclusions at the

518 source of non-exponential transverse relaxation in subcortical brain regions (Bauer and Nadler, 2002;

519 Ziener et al., 2005). Moreover, brain tissue is inherently complex, involving a distribution of inclusions

520 with varied sizes and susceptibilities originating from different cell types and structures. Some of these

521 inclusions, such as larger cells like neurons, might be better described by the SDR, while others, such

522 as smaller cells like glia, might be better described by the DNR. Additionally, the different models of

523 the MRI signal considered here led to systematic differences in the estimates of the magnetic

524 inclusions. Alternative models of the effect of the inclusions on the MRI signal should therefore be

525 considered.

526 Future quantitative histological studies on cellular iron distributions in different subcortical areas may

527 provide valuable priors for an informed choice of the appropriate model. In combination with the

528 presented acquisition and fitting approach, this could enable the extraction of cellular characteristics

529 non-invasively from non-exponential MR relaxometry.

530 **5.3   Non-heme iron as a possible source of the non-exponential signal decay**

531 Previous studies have suggested that the quadratic behaviour of non-heme iron may only be

532 detectable at echo times well below 1 ms, below the range of achievable echo times, because clusters

533 of non-heme iron were taken to be smaller than ~100 nm (Yablonskiy et al., 2021). As a result, non-

534 exponential signal decay was attributed to heme iron in deoxygenated blood. However, the results of

535 the numerical simulations presented here (Figure 6) show that, in the SN, iron-rich dopaminergic

536 neurons ~15 μm in size can lead to non-exponential decay in gradient-echo data acquired within a

537 conventional range of echo times.

538 Additionally, while other magnetic materials like myelin or blood vessels also contribute to the non-
539 exponential behaviour, the strongest deviations from the exponential decay occur in regions with high
540 non-heme iron content (Section 5.1). This result further highlights the impact of cells rich in non-heme
541 iron on the observed non-exponential decay behaviour.

542 **6   Conclusions**

543 In this study, we provided experimental evidence of non-exponential transverse relaxation signal
544 decay in in vivo gradient-echo MRI data from subcortical brain regions at 3T. The behaviour of the
545 decay is consistent with the effect of magnetic inclusions on the MRI signal predicted by theoretical
546 studies. These theoretical models of the MRI signal yield improved fit with experimental data
547 compared to the widely used exponential model. The larger deviations from exponential decay were
548 observed in iron-rich subcortical regions (substantia nigra, globus pallidus). The experimental and
549 numerical results presented here suggest that the observed non-exponential signal decay may
550 originate from cells rich in non-heme iron such as dopaminergic neurons in the substantia nigra. From
551 the estimates of the model parameters, we attempted to characterize the size, volume fraction and
552 magnetic susceptibility of these cells. Non-exponential transverse relaxation signal decay provides
553 new opportunities for the study of iron-related changes in neurodegenerative diseases non-invasively
554 from MRI data, with increased specificity.

555 **7   Conflict of Interest**

556 The authors declare no conflict of interest.

557 **8   Author Contributions**

558 RO: Conceptualization, Methodology, Investigation, Formal analysis, Writing-Original draft, Writing –
559 Review and Editing, QR: Investigation, Writing – Review and Editing, EK: Investigation,
560 Conceptualization, Writing – Review & Editing, VGK: Conceptualization, Writing – Review & Editing,
561 IJ: Conceptualization, Writing – Review & Editing, AL: Conceptualization, Methodology, Investigation,
562 Formal analysis, Writing-Original draft, Writing – Review and Editing, Supervision, Project
563 administration, Funding acquisition.

564 **9   Funding**

568 **10   Data and code availability**

569   The code and data used for this analysis will be made publicly available upon publication.

570   **11   References**

571   Anderson, P. W., and Weiss, P. R. (1953). Exchange Narrowing in Paramagnetic Resonance. *Exch.*
572   *Organ. Behav. Teach. J.* 679.

573   Ashburner, J., and Friston, K. J. (2005). Unified segmentation. *Neuroimage* 26, 839–851. doi:
574   10.1016/j.neuroimage.2005.02.018.

575   Barber, T. W., Brockway, J. A., and Higgins, L. S. (1970). The density of tissues in and about the
576   head. *Acta Neurol. Scandinav.* 46, 85-92,.

577   Bauer, W. R., and Nadler, W. (2002). Spin dephasing in the extended strong collision approximation.
578   *Phys. Rev. E - Stat. Physics, Plasmas, Fluids, Relat. Interdiscip. Top.* 65, 1–15. doi:
579   10.1103/PhysRevE.65.066123.

580   Brammerloh, M., Morawski, M., Friedrich, I., Reinert, T., Lange, C., Pelicon, P., et al. (2021).
581   Measuring the iron content of dopaminergic neurons in substantia nigra with MRI relaxometry.
582   *Neuroimage* 239, 118255. doi: 10.1016/j.neuroimage.2021.118255.

583   Brammerloh, M., Sibgatulin, R., Herrmann, K. H., Morawski, M., Reinert, T., Jäger, C., et al. (2024).
584   In Situ Magnetometry of Iron in Human Dopaminergic Neurons Using Superresolution MRI and
585   Ion-Beam Microscopy. *Phys. Rev. X* 14, 21041. doi: 10.1103/PhysRevX.14.021041.

586   Castella, R., Arn, L., Dupuis, E., Callaghan, M. F., Draganski, B., and Lutti, A. (2018). Controlling
587   motion artefact levels in MR images by suspending data acquisition during periods of head
588   motion. *Magn. Reson. Med.* 80, 2415–2426. doi: 10.1002/mrm.27214.

589   Corbin, N., Oliveira, R., Raynaud, Q., Di Domenicantonio, G., Draganski, B., Kherif, F., et al. (2023).
590   Statistical analyses of motion-corrupted MRI relaxometry data computed from multiple scans. *J.*
591   *Neurosci. Methods* 398. doi: 10.1016/j.jneumeth.2023.109950.

592   Damulina, A., Pirpamer, L., Soellradl, M., Sackl, M., Tinauer, C., Hofer, E., et al. (2020). Cross-
593   sectional and longitudinal assessment of brain iron level in Alzheimer disease using 3-T MRI.
594   *Radiology* 296, 619–626. doi: 10.1148/radiol.2020192541.

595   Does, M. D., Olesen, J. L., Harkins, K. D., Serradas-Duarte, T., Gochberg, D. F., Jespersen, S. N.,
596   et al. (2019). Evaluation of principal component analysis image denoising on multi-exponential
597   MRI relaxometry. *Magn. Reson. Med.* 81, 3503–3514. Available at:
598   https://onlinelibrary.wiley.com/doi/full/10.1002/mrm.27658.

599   Friedrich, I., Reimann, K., Jankuhn, S., Kirilina, E., Stieler, J., Sonntag, M., et al. (2021). Cell specific
600   quantitative iron mapping on brain slices by immuno-µPIXE in healthy elderly and Parkinson's
601   disease. *Acta Neuropathol. Commun.* 9, 1–17. doi: 10.1186/s40478-021-01145-2.

602   Fukunaga, M., Li, T. Q., Van Gelderen, P., De Zwart, J. A., Shmueli, K., Yao, B., et al. (2010). Layer-
603   specific variation of iron content in cerebral cortex as a source of MRI contrast. *Proc. Natl.*

604   *Acad. Sci. U. S. A.* 107, 3834–3839. doi: 10.1073/pnas.0911177107.

605   Gerlach, M., Ben-Shachar, D., Riederer, P., and Youdim, M. B. H. (1994). Altered brain metabolism
606   of iron as a cause of neurodegenerative diseases? *J. Neurochem.* 63, 793–807. doi:
607   10.1046/j.1471-4159.1994.63030793.x.

608   Griffiths, P. D., Dobson, B. R., Jones, G. R., and Clarke, D. T. (1999). Iron in the basal ganglia in
609   Parkinson's disease. An in vitro study using extended X-ray absorption fine structure and cryo-
610   electron microscopy. *Brain* 122, 667–673. doi: 10.1093/brain/122.4.667.

611   Haacke, E. M., Cheng, N. Y. C., House, M. J., Liu, Q., Neelavalli, J., Ogg, R. J., et al. (2005).
612   Imaging iron stores in the brain using magnetic resonance imaging. *Magn. Reson. Imaging* 23,
613   1–25. doi: 10.1016/j.mri.2004.10.001.

614   Hallgren, B., and Sourander, P. (1958). The effect of age on non-haemin iron in the human brain. *J.*
615   *Neurochem.* 3, 41–51. doi: 10.1136/jnnp.50.2.231.

616   Hare, D., Ayton, S., Bush, A., and Lei, P. (2013). A delicate balance: Iron metabolism and diseases
617   of the brain. *Front. Aging Neurosci.* 5, 1–19. doi: 10.3389/fnagi.2013.00034.

618   Helms, G., Dathe, H., and Dechent, P. (2008a). Quantitative FLASH MRI at 3T using a rational
619   approximation of the Ernst equation. *Magn. Reson. Med.* 59, 667–672. doi:
620   10.1002/mrm.21542.

621   Helms, G., Dathe, H., Kallenberg, K., and Dechent, P. (2008b). High-resolution maps of
622   magnetization transfer with inherent correction for RF inhomogeneity and T1 relaxation
623   obtained from 3D FLASH MRI. *Magn. Reson. Med.* 60, 1396–1407. doi: 10.1002/mrm.21732.

624   Helms, G., Draganski, B., Frackowiak, R., Ashburner, J., and Weiskopf, N. (2009). Improved
625   segmentation of deep brain grey matter structures using magnetization transfer (MT) parameter
626   maps. *Neuroimage* 47, 194–198. doi: 10.1016/j.neuroimage.2009.03.053.

627   Jensen, J. H., and Chandra, R. (2000a). NMR relaxation in tissues with weak magnetic
628   inhomogeneities. *Magn. Reson. Med.* 44, 144–156. doi: 10.1002/1522-
629   2594(200007)44:1<144::AID-MRM21>3.0.CO;2-O.

630   Jensen, J. H., and Chandra, R. (2000b). Strong field behavior of the NMR signal from magnetically
631   heterogeneous tissues. *Magn. Reson. Med.* 43, 226–236. doi: 10.1002/(SICI)1522-
632   2594(200002)43:2<226::AID-MRM9>3.0.CO;2-P.

633   Kennan, R. P., Zhong, J., and Gore, J. C. (1994). Intravascular susceptibility contrast mechanisms
634   in tissues. *Magn. Reson. Med.* 31, 9–21. doi: 10.1002/mrm.1910310103.

635   Kirilina, E., Helbling, S., Morawski, M., Pine, K., Reimann, K., Jankuhn, S., et al. (2020). Superficial
636   white matter imaging: Contrast mechanisms and whole-brain in vivo mapping. *Sci. Adv.* 6, 1–
637   14. doi: 10.1126/sciadv.aaz9281.

638   Kiselev, V. G., and Novikov, D. S. (2002). Transverse NMR Relaxation as a Probe of Mesoscopic
639   Structure. *Phys. Rev. Lett.* 89, 2–5. doi: 10.1103/PhysRevLett.89.278101.

640   Kiselev, V. G., and Novikov, D. S. (2018). Transverse NMR relaxation in biological tissues.
641   *Neuroimage* 182, 149–168. doi: 10.1016/j.neuroimage.2018.06.002.

642   Krebs, N., Langkammer, C., Goessler, W., Ropele, S., Fazekas, F., Yen, K., et al. (2014).
643   Assessment of trace elements in human brain using inductively coupled plasma mass
644   spectrometry. *J. Trace Elem. Med. Biol.* 28, 1–7. doi: 10.1016/j.jtemb.2013.09.006.

645   Langkammer, C., Krebs, N., Goessler, W., Scheurer, E., Ebner, F., Yen, K., et al. (2010).
646   Quantitative MR imaging of brain iron: A postmortem validation study. *Radiology* 257, 455–462.
647   doi: 10.1148/radiol.10100495.

648   Langkammer, C., Schweser, F., Krebs, N., Deistung, A., Goessler, W., Scheurer, E., et al. (2012).
649   Quantitative susceptibility mapping (QSM) as a means to measure brain iron? A post mortem
650   validation study. *Neuroimage* 62, 1593–1599. doi: 10.1016/j.neuroimage.2012.05.049.

651   Lauwers, F., Cassot, F., Lauwers-Cances, V., Puwanarajah, P., and Duvernoy, H. (2008).
652   Morphometry of the human cerebral cortex microcirculation: General characteristics and space-
653   related profiles. *Neuroimage* 39, 936–948. doi: 10.1016/j.neuroimage.2007.09.024.

654   Lutti, A., Corbin, N., Ashburner, J., Ziegler, G., Draganski, B., Phillips, C., et al. (2022). Restoring
655   statistical validity in group analyses of motion- corrupted MRI data. *Hum. Brain Mapp.*, 1–11.
656   Available at: 10.1002/hbm.25767.

657   Lutti, A., Hutton, C., Finsterbusch, J., Helms, G., and Weiskopf, N. (2010). Optimization and
658   validation of methods for mapping of the radiofrequency transmit field at 3T. *Magn. Reson.*
659   *Med.* 64, 229–238. doi: 10.1002/mrm.22421.

660   Lutti, A., Stadler, J., Josephs, O., Windischberger, C., Speck, O., Bernarding, J., et al. (2012).
661   Robust and fast whole brain mapping of the RF transmit field B1 at 7T. *PLoS One* 7, 1–7. doi:
662   10.1371/journal.pone.0032379.

663   Maclaren, J., Armstrong, B. S. R., Barrows, R. T., Danishad, K. A., Ernst, T., Foster, C. L., et al.
664   (2012). Measurement and Correction of Microscopic Head Motion during Magnetic Resonance
665   Imaging of the Brain. *PLoS One* 7, 3–11. doi: 10.1371/journal.pone.0048088.

666   Möller, H. E., Bossoni, L., Connor, J. R., Crichton, R. R., Does, M. D., Ward, R. J., et al. (2019). Iron
667   , Myelin , and the Brain : Neuroimaging Meets Neurobiology. *Trends Neurosci.* 42, 384–401.
668   doi: 10.1016/j.tins.2019.03.009.

669   Novikov, D. S., and Kiselev, V. G. (2008). Transverse NMR relaxation in magnetically
670   heterogeneous media. *J. Magn. Reson.* 195, 33–39. doi: 10.1016/j.jmr.2008.08.005.

671   Novikov, D. S., Kiselev, V. G., and Jespersen, S. N. (2018). On modeling. *Magn. Reson. Med.* 79,
672   3172–3193. doi: 10.1002/mrm.27101.

673   Péran, P., Cherubini, A., Luccichenti, G., Hagberg, G., Démonet, J. F., Rascol, O., et al. (2009).
674   Volume and iron content in basal ganglia and thalamus. *Hum. Brain Mapp.* 30, 2667–2675. doi:
675   10.1002/hbm.20698.

676 Raynaud, Q., Domenicantonio, G. Di, Yerly, J., Dardano, T., Heeswijk, R. B. van, and Lutt, A.
677   (2023). A characterization of cardiac-induced noise in R2* maps of the brain. *Magn. Reson.*
678   *Med.*, 1–15. doi: 10.2307/2318215.

679 Reinert, A., Morawski, M., Seeger, J., Arendt, T., and Reinert, T. (2019). Iron concentrations in
680   neurons and glial cells with estimates on ferritin concentrations. *BMC Neurosci.* 20, 1–14. doi:
681   10.1186/s12868-019-0507-7.

682 Schweser, F., Deistung, A., Lehr, B. W., and Reichenbach, J. R. (2011). Quantitative imaging of
683   intrinsic magnetic tissue properties using MRI signal phase: An approach to in vivo brain iron
684   metabolism? *Neuroimage* 54, 2789–2807. doi: 10.1016/j.neuroimage.2010.10.070.

685 Sedlacik, J., Boelmans, K., Löbel, U., Holst, B., Siemonsen, S., and Fiehler, J. (2014). Reversible,
686   irreversible and effective transverse relaxation rates in normal aging brain at 3T. *Neuroimage*
687   84, 1032–1041. doi: 10.1016/j.neuroimage.2013.08.051.

688 Storey, P., Chung, S., Ben-Eliezer, N., Lemberskiy, G., Lui, Y. W., and Novikov, D. S. (2015).
689   Signatures of Microstructure in Conventional Gradient and Spin Echo Signals. in *Proc. 23rd*
690   *Annual Meeting ISMRM, Toronto, Canada*, 014.

691 Stüber, C., Morawski, M., Schäfer, A., Labadie, C., Wähnert, M., Leuze, C., et al. (2014). Myelin and
692   iron concentration in the human brain: A quantitative study of MRI contrast. *Neuroimage* 93,
693   95–106. doi: 10.1016/j.neuroimage.2014.02.026.

694 Sukstanskii, A. L., and Yablonskiy, D. A. (2003). Gaussian approximation in the theory of MR signal
695   formation in the presence of structure-specific magnetic field inhomogeneities. *J. Magn. Reson.*
696   163, 236–247. doi: 10.1016/S1090-7807(03)00131-9.

697 Tabelow, K., Balteau, E., Ashburner, J., Callaghan, M. F., Draganski, B., Helms, G., et al. (2019).
698   hMRI – A toolbox for quantitative MRI in neuroscience and clinical research. *Neuroimage* 194,
699   191–210. doi: 10.1016/j.neuroimage.2019.01.029.

700 Thompson, K. J., Shoham, S., and Connor, J. R. (2001). Iron and neurodegenerative disorders.
701   *Brain Res. Bull.* 55, 155–164. doi: 10.1016/S0361-9230(01)00510-X.

702 Ulla, M., Bonny, J. M., Ouchchane, L., Rieu, I., Claise, B., and Durif, F. (2013). Is R2* a New MRI
703   Biomarker for the Progression of Parkinson's Disease? A Longitudinal Follow-Up. *PLoS One* 8,
704   1–8. doi: 10.1371/journal.pone.0057904.

705 Ulrich, X., and Yablonskiy, D. A. (2016). Separation of cellular and BOLD contributions to T2* signal
706   relaxation. *Magn. Reson. Med.* 75, 606–615. doi: 10.1002/mrm.25610.

707 Veraart, J., Fieremans, E., and Novikov, D. S. (2016a). Diffusion MRI noise mapping using random
708   matrix theory. *Magn. Reson. Med.* 76, 1582–1593. doi: 10.1002/mrm.26059.

709 Veraart, J., Novikov, D. S., Christiaens, D., Ades-aron, B., Sijbers, J., and Fieremans, E. (2016b).
710   Denoising of diffusion MRI using random matrix theory. *Neuroimage* 142, 394–406. doi:
711   10.1016/j.neuroimage.2016.08.016.

712 Ward, R. J., Zucca, F. A., Duyn, J. H., Crichton, R. R., and Zecca, L. (2014). The role of iron in brain
713   ageing and neurodegenerative disorders. *Lancet Neurol.* 13, 1045–1060. doi: 10.1016/S1474-
714   4422(14)70117-6.

715 Weiskopf, N., Callaghan, M. F., Josephs, O., Lutti, A., and Mohammadi, S. (2014). Estimating the
716   apparent transverse relaxation time (R2*) from images with different contrasts (ESTATICS)
717   reduces motion artifacts. *Front. Neurosci.* 8, 1–10. doi: 10.3389/fnins.2014.00278.

718 Weiskopf, N., Suckling, J., Williams, G., Correia M., M. M., Inkster, B., Tait, R., et al. (2013).
719   Quantitative multi-parameter mapping of R1, PD*, MT, and R2* at 3T: A multi-center validation.
720   *Front. Neurosci.* 7, 1–11. doi: 10.3389/fnins.2013.00095.

721 Yablonskiy, D. A., and Haacke, E. M. (1994). Theory of NMR signal behavior in magnetically
722   inhomogeneous tissues: The static dephasing regime. *Magn. Reson. Med.* 32, 749–763. doi:
723   10.1002/mrm.1910320610.

724 Yablonskiy, D. A., Sukstanskii, A. L., Luo, J., and Wang, X. (2013). Voxel spread function method for
725   correction of magnetic field inhomogeneity effects in quantitative gradient-echo-based MRI.
726   *Magn. Reson. Med.* 70, 1283–1292. doi: 10.1002/mrm.24585.

727 Yablonskiy, D. A., Wen, J., Kothapalli, S. V. V. N., and Sukstanskii, A. L. (2021). In vivo evaluation
728   of heme and non-heme iron content and neuronal density in human basal ganglia. *Neuroimage*
729   235, 118012. doi: 10.1016/j.neuroimage.2021.118012.

730 Yao, B., Li, T. Q., Gelderen, P. van, Shmueli, K., de Zwart, J. A., and Duyn, J. H. (2009).
731   Susceptibility contrast in high field MRI of human brain as a function of tissue iron content.
732   *Neuroimage* 44, 1259–1266. doi: 10.1016/j.neuroimage.2008.10.029.

733 Zaitsev, M., Dold, C., Sakas, G., Hennig, J., and Speck, O. (2006). Magnetic resonance imaging of
734   freely moving objects: prospective real-time motion correction using an external optical motion
735   tracking system. *Neuroimage* 31, 1038–1050. doi: 10.1016/j.neuroimage.2006.01.039.

736 Ziener, C. H., Bauer, W. R., and Jakob, P. M. (2005). Transverse relaxation of cells labeled with
737   magnetic nanoparticles. *Magn. Reson. Med.* 54, 702–706. doi: 10.1002/mrm.20634.
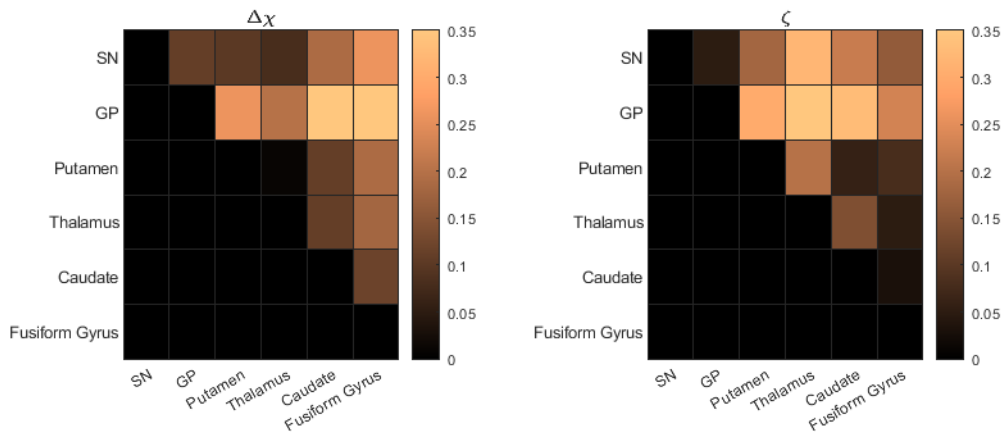
738
739

12   Supplementary
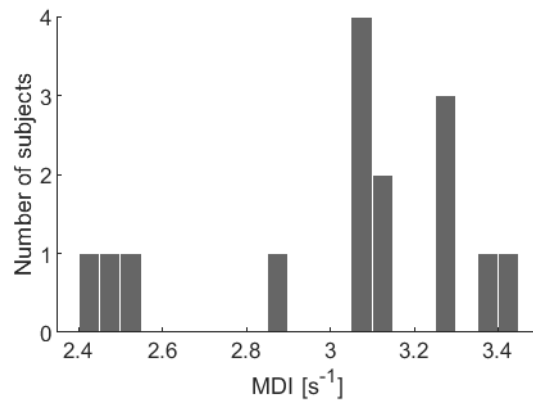
Figure S1. Distribution of Motion Degradation Index (MDI) across subjects and repetitions.

Figure S2. Absolute effect size (cliff's delta) of the differences in $\Delta\chi$ and ζ between subcortical regions for the AW models. A value of 0 suggests no difference between the two regions, while values closer to 1 indicate stronger associations. The p-values are not shown given that excluding the pair thalamus and putamen in $\Delta\chi$, all the remaining pairwise comparisons were significant (due to the large sample size). Note that given that the matrix is symmetric only the upper part is shown.

26